Nonuniformity Correction Method of Infrared Detector Based on Statistical Properties

Li Dandan, Ding Xiang, Chai Mengyang, Ma Chao, and Sun Dexin, *Member, IEEE*

***Abstract*—The images captured by a plane-array type infrared detector, formed by integrating a large-scale probe array and readout circuits via interconnection, is distorted by two types of superimposed nonuniform noises caused by the probe and readout circuitry. These nonuniform noises arise from the detector's constituent materials, fabrication processes, and other defects. In addition, the output response of an infrared detector is limited by the dynamic range of the circuit, the low and high ends of the output signal exhibit strong nonlinearities. To overcome the impact of detector response nonlinearity and achieve simultaneous correction for two different types of nonuniformities in infrared images, in this study, we proposed a novel correction method. First, the pixel points of all images are reordered according to their pixel values to provide a uniform reorganisation data. Then, the linear correlated region based on the recombined data is extracted using a judgment algorithm that processes the linear correlations of multiple regions to simulate the detector's response curve and find the nonuniformity correction coefficient of each pixel. Experiments on simulated noisy and real images show that our method accurately eliminates nonuniform IR noise without causing blurring and provides optimal peak signal-to-noise ratio and structural similarity.**

***Index Terms*—Infrared detector, nonuniformity noise, correction, focal-plane detector array, readout, nonlinearities.**

I. Introduction

INFRARED (IR) imaging technologies support a wide range of ecological emergency management requirements. However, the limitations of detection materials and fabrication processes have led to inconsistent detector outputs and image quality. To over-come these problems, researchers have proposed a variety of calibration correction methods based on a standard radiation source [1], [2]. The basis of this method is to measure the responses of IR focal plane detectors using a standard uniform radiating source at a fixed temperature and determine nonuniformity compensation (NUC) co-efficients using two- or multi-point methods. However, the calibration coefficients of detectors change over time, requiring the operation to be carried out with extended periodicity, which limits the normal operational availability of IR systems. Moreover, detector responses are nonlinear, and the success of calibration diminishes with severity. Another method automatically calculates calibration coefficients in real time based on the scene and updates the corresponding coefficients [3], [4], [5] without affecting the normal operational requirements of the instrument.

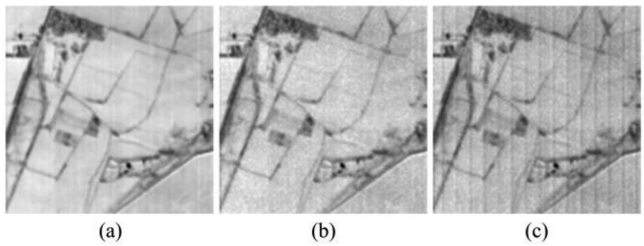

Fig. 1. (a) Original image. (b) Noise generated by different probes. (c) Noise generated by different readout circuits and probes.

Two-dimensional IR focal plane-array detectors capture entire full-surface scenes using interconnected probe elements [6] that convert IR radiation into electrical signals. However, the necessary semiconductor materials inevitably suffer from nonuniformities in processing dimensions and doping concentrations, resulting in physical parametric inconsistencies in response to radiation inputs, even from similar homogeneous regions [7]. This phenomenon is known as "sand noise" and is illustrated in Fig. 1(b).

To ensure the efficient operation of IR detectors, their focal plane readout circuits require multiple parallel transmissions. However, the circuits of different output stag-es use different parameters, which directly lead to inhomogeneities in output signals [6]. This phenomenon is known as "stripe noise" [8] and is shown in Fig. 1(c).

Therefore, focal plane array infrared images are affected by the superposition of two types of nonuniform noise introduced by the probe elements and readout circuit. Many correction methods have been proposed to address these two types of nonuniform noise. Esteban and colleagues proposed an adaptive scene-based nonuniformity correction method, experiments

Manuscript received 21 October 2023; revised 12 February 2024; accepted 17 February 2024. Date of publication 20 February 2024; date of current version 14 March 2024. This work was supported in part by the Major Program of the National Natural Science Foundation of China under Grant 42192582, in part by the National Key R&D Program of China under Grant 2022YFB3902000, and in part by the Youth Innovation Promotion Association CAS under Grant 2023246 and Grant 2020242. *(This work is mainly completed by Li Dandan.) (Corresponding author: Sun Dexin.)*

Li Dandan and Sun Dexin are with the State Key Laboratory of Infrared Physics, Shanghai Institute of Technical Physics, Chinese Academy of Sciences, Shanghai 200083, China, and also with the University of Chinese Academy of Sciences, Beijing 100049, China (e-mail: lidandan@mail.sitp.ac.cn; sun dexin@mail.sitp.ac.cn).

Ding Xiang is with the Beijing Institute of Tracking and Telecommunication Technology, Beijing 100049, China (e-mail: dingxiang1212@163.com).

Chai Mengyang and Ma Chao are with the State Key Laboratory of Infrared Physics, Shanghai Institute of Technical Physics, Chinese Academy of Sciences, Shanghai 200083, China (e-mail: mengyang9999@126.com; seuedumc @163.com).

Digital Object Identifier 10.1109/JPHOT.2024.3367997

demonstrate that this method can effectively correct nonuniform noise from the readout circuit. However, the correction results may introduce some ghosting artifacts, which impact the image quality [9]. Russell first introduced a scene-based registration algorithm for readout circuit nonuniformity correction, this algorithm primarily relies on the unique response characteristics of each probe element. However, the accuracy of scene motion estimation significantly affects the precision of registration-based nonuniformity correction algorithms [10]. Tendero proposed a nonuniform stripe noise correction algorithm based on histogram equalization, the core idea of the algorithm is to use an equalization function to adjust the brightness distribution of the image to eliminate nonuniform responses. Although histogram equalization can improve image nonuniformity, it may introduce other types of noise [3]. Cao and colleagues proposed a nonuniform stripe noise correction algorithm based on a 1D row-guided filter, experiments show that this algorithm can denoise images without blurring the details. However, for images with a large number of horizontal and vertical edges, the algorithm may lose some edge details in the image [4]. Zhuang proposed a novel stripe nonuniformity correction algorithm based on accelerated robust feature extraction, this algorithm is a registration-based correction method capable of overcoming image registration issues caused by rotation and affine transformations of images. However, this method is still affected by the accuracy of scene motion estimation [11]. In summary, many superior methods have been proposed for correcting single types of nonuniform noise. But current research lacks methods capable of correcting both types of noise simultaneously.

To overcome this problem, this study proposes a new scene-based NUC correction method that analyses the process and nature of nonuniform noise generation based on the fact that the response output of one probe element is consistent for the same radiant energy input over a short period. Multiple IR image frames are acquired to render uniform regions based on pixel values, followed by the construction of a multi-segmented linear model using these regions to approximate the nonlinear response curves of the detectors. Then, the multi-segmented two-point method is used to derive the NUC coefficients of the different detectors. Response curve approximation is achieved by increasing the number of linear models in response to the severity of detector nonlinearity. Therefore, our method can correct both probe noise and readout circuit noise in images without losing image details. Additionally, this algorithm does not require image registration; it only needs to arrange images acquired over a period of time in chronological order into a set of three-dimensional data. The main contributions of this study are summarized as follows:

- Our statistical characterization method for nonuniform IR images simultaneously eliminates the two types of noise caused by readout circuits and detector arrays;
- The causes of nonuniform noise are comprehensively analyzed to provide a theoretical basis for future research;
- Comparison experiments on simulated and real nonuniform noise data show that the method proposed has high restoration quality.

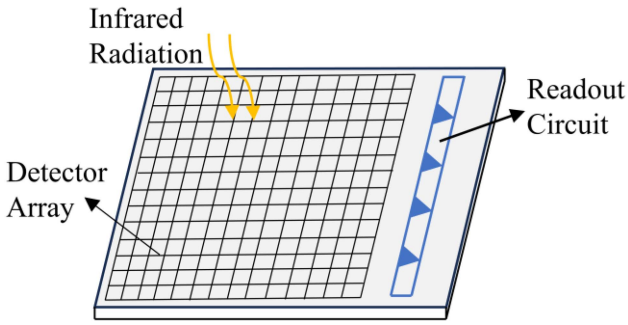

Fig. 2. Infrared outer array detector.

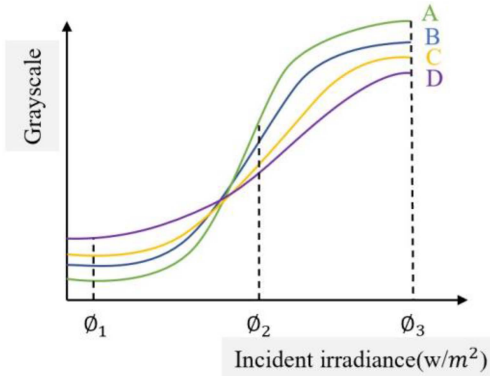

Fig. 3. S-type response curves. A, B, C, and D on the right represent the response characteristic curves of different probes.

The remainder of this paper is organized as follows. In Section II, we explain nonuniform noise and current correction methods. In Section III, the proposed method is described in detail. In Section IV, our results are analyzed and compared with other methods, and conclusions are presented in Section V.

II. Related Work

There are two main types of nonuniform image noise produced by array detectors and their readout circuitry. Fig. 2 shows the structure of a typical detector. Zhuang et al. demonstrated through experiments that within an effective input range, the response of the detector's pixels and readout circuitry is nonlinear and approximates an 'S' type curve [11], [12]. Fig. 3 illustrates the horizontal coordinates of incident irradiance and the vertical coordinates of converted output voltage. The curve varies based on the probe, which exacerbates the nonuniformity in the form of sand noise (Fig. 1(b)). Although this noise can be relatively weak at first glance, it interferes with data processing and analysis after image manipulation. Owing to the large size of typical IR focal plane detector arrays and the number of probes, multiple readout circuits are usually adopted to transmit signals to an output module in a certain order [13]. Hence, the same column of probes usually uses the same readout circuit, and their specific 'S' type curve shapes differ, leading to image stripe noise (Fig. 1(c)). These response inconsistencies cause different gain and bias

coefficients for each probe [14]. Interestingly, this superposition of probs and readout circuit nonuniformities causes a "stripe and sand" noise to appear, also shown in Fig. 1(c).

Generally, the S-type response curves of probe and readout circuits exhibit similar characteristics of a slow rise followed by a rapid increase followed by saturation [12]. The theoretical 'S' type curve can be modelled as follows:

$$DN_{i,j}(n) = \frac{A_{i,j}(n)}{1 + e^{B_{i,j}(n)\emptyset_{i,j}(n) + C_{i,j}(n)}} + D_{i,j}(n). \quad (1)$$

where $\emptyset_{i,j}(n)$ and $DN_{i,j}(n)$ denote the irradiation input and response output of the (i, j) probe element at the *n*th moment, respectively. $A_{i,j}(n)$, $B_{i,j}(n)$, $C_{i,j}(n)$, and $D_{i,j}(n)$ are the probe element response curve parameters, where $D_{i,j}(n)$ is the dark current noise. Owing to the limitations of manufacturing processes, these parameters can differ considerably, despite their similarities.

Regarding sand noise, Esteban et al. proposed a full variance adaptive correction method based on image sequences [9]. However, this technique is prone to localized motion artifacts. To overcome this problem, Yoonsung et al. applied an effective Kalman filtering algorithm [15]. Based on the spectral properties of nonuniform noise, scholars have proposed several de-striping methods [4], [16], [17], [18] that usually apply threshold parameters to differentiate edges from noise to avoid blurring. However, these methods can erroneously remove weak image edges while retaining strong stripe noise artifacts.

With the rapid development of artificial neural networks, deep learning methods have provided impressive image nonuniform denoising results [8], [19], [20] that do not result in image blurring. However, most methods transitionally optimize images, and even the most outstanding results [21], [22], [23] ignore the superimposition of both sand and stripe noises.

III. Method

Our method approximates the 'S' type curve of the detector using a combination of multiple linear models based on regions of nonlinearity at low and high response levels. As such, this method can fit a variety of response curves. The response DN value and its irradiance input, $\emptyset$, satisfy a multi-segmented linear relationship, given by the following equation:

$$DN_n(i, j) = a_n(i, j) \times \emptyset_n(i, j) + b_n(i, j) \quad (2)$$

where $\emptyset_n(i, j)$ is the irradiation probe element input at the *n*th segment (i, j), $DN_n(i, j)$ is the response output of the probe element, $a_n(i, j)$ is the gain coefficient and $b_n(i, j)$ is the bias coefficient. The gain and bias coefficients for each pixel are computed from two data segments consisting of relatively dark and light pixel values.

It is known that the gain and bias coefficients of each pixel acquired by the surface array detector differ. However, they remain the same over short periods. Most detectors use 10–50-Hz frame rates and can acquire thousands of images in a short period. Our method requires a sufficiently large number of images taken over a short period so that they can be combined into sets of three-dimensional (3D) data cubes, as shown in Fig. 4: Step 1.

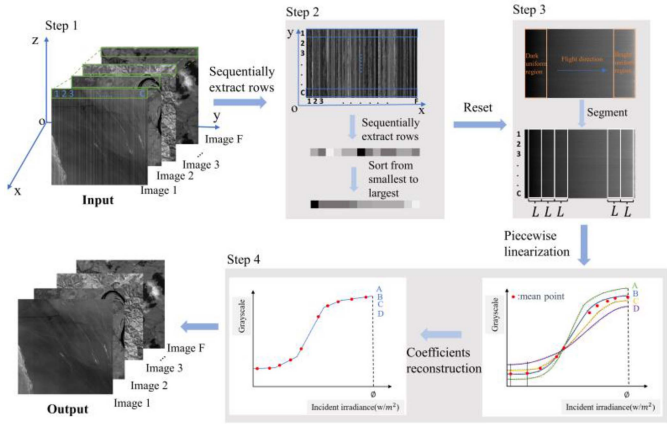

Fig. 4. Processing workflow of the proposed method.

The yoz-plane is the spatial dimension of the image, the x-axis is the direction of the frame dimension and the number of frames is F. From the reconstructed 3D images, data from each row is sequentially extracted to form a two-dimensional plane (xoy plane). In the xoy plane, each row of data has the same gain and bias coefficients.

For the extracted xoy surface, each row of pixel values is sorted from smallest to largest, and the xoy surface is partitioned into *n* homogeneous regions according to their grey-value variations, each of size $L \times C$, as shown in Fig. 4: Step 3. The average *DN* value of the *n*th uniform block region is denoted by T_n, $n = 1, 2, 3 \ldots N$:

$$T_n = \frac{1}{L \times C} \sum_{i=(n-1)\times L+1}^{n\times L} \sum_{j=1}^{C} DN(i, j). \quad (3)$$

The average value of $Q_n(c)$ of the *c*th row of the *n*th uniform region, where $c = 1, 2, 3 \ldots C$ and $n = 1, 2, 3 \ldots N$, is denoted as:

$$Q_n(c) = \frac{1}{L} \sum_{i=(n-1)\times L+1}^{n\times L} DN(i, c). \quad (4)$$

If the difference in means between consecutive neighbouring homogeneous regions, D_V_{n-1}, is equal, the regions are considered to exist in the same section of the linear model. Hence, the expression of D_V_{n-1} is provided as follows:

$$D\_V_{n-1} = T_n - T_{n-1} \quad (5)$$

Taking an image grey value range of [0, 4095] as an example, the fluctuation between D_V_{n-1} and D_V_{n-2} is within [0, 10]. Thus, it is considered that D_V_{n-1} and D_V_{n-2} are in the same segment of the linear model. It follows that the uniform region within the linear segment is not fixed.

We assume that the S-curve is divided into H segments, each containing m uniform regions. Hence, the gain and bias coefficients can be obtained by selecting the dark and bright uniform regions, where a and b are constants determined based

on the size of m:

$$\begin{cases} 1 \text{ and } m,\ 2 \le m \le 3 \\ a \text{ and } m-a+1,\ m = 2a+b\ a > 1,\ b \ge a \end{cases} \tag{6}$$

The NUC coefficients of the pixels in each segment of the linear model are then calculated using the following equation:

$$\begin{cases} k\left(i,j\right) \times Q_1\left(i\right) + b\ \ (i,j) = T_1 \\ k\left(i,j\right) \times Q_2\left(i\right) + b\ \ (i,j) = T_2 \end{cases} \tag{7}$$

where $i = 1, 2, 3 \ldots H$, and $j = 1, 2, 3 \ldots N$. $Q_1(i)$ and $Q_2(i)$ represent the mean values on row i in the two homogeneous regions selected under the linear model. T_1 and T_2 are the mean values of the two homogeneous regions selected using a linear model.

This process provides the NUC coefficients of each line of each segment in the uniform region of the xoy-plane, and the NUC coefficients of the S-curve's pixel point are determined based on its row. Subsequently, the point's grey value is used to determine the linear model (uniform region) segment on the S-curve, where the pixel point is located between the model's brightest uniform region mean value, T_{n1}, and the darkest uniform region mean value, T_{n2}. Finally, each pixel is corrected according to the NUC coefficients of the corresponding segment.

Homogeneous areas have similar reflected irradiance features, and current IR detectors are generally characterised by high frame rates; hence, they can capture thousands of IR images over a short period, during which the response characteristics of the detector remain essentially stable. Furthermore, consecutive multi-frame shooting can acquire many IR images within a given feature area to fulfil the need to obtain features with similar reflective irradiances. Because the output *DN* value has a nonlinear relationship with the irradiance reflected from a ground object, sorting the acquired *DN* values involves evaluating the reflected irradiances. After a sufficient number of IR images are collected, pixel points at the same detector location for all images are arranged in order of size, and features having similar reflective irradiances are clustered into a single area. This process utilises the response properties of detectors and the statistical properties of ground objects based on a sufficiently large number of images. Hence, our NUC process remains independent of particular scenes.

The experimental procedure for the proposed method is illustrated in Fig. 4. Step 1: the acquired IR images are arranged into a 3D data cube based on probe locations. Step 2: (a). the same rows of data for each image are extracted and arranged into a 2D dataset; (b). the data in each 2D row are reordered into an ascending order. Step 3: (a). to minimise the effects of irregular saturation and bad pixels, the top and bottom 10 columns are discarded and the remaining *DN* values are retained as valid data; (b). the sorted and valid data are partitioned into homogeneous regions according to the number of *DN*s per L. Note that L was set to 20 for our experiment. The mean value, T_n, is then calculated for each region, and the mean value, $Q_n(c)$, is calculated for each row in each block area. Step 4: (a). the range of each linear model is divided according to the mean difference of the proximity region, D_V_{n-1}, and the appropriate bright and dark uniform regions are selected to produce the NUC coefficients; (b). each pixel point is corrected by determining the corresponding NUC coefficients according to its position and size. Finally, the process is complete.

IV. Experimental Results and Discussion

In this section, we first introduce our evaluation metrics. Then, our dataset is presented. Note that our experiment used real IR images, including simulated nonuniform noise images and data collected by our detector. We also compare the correction effects of our method with four other state-of-the-art NUC methods: midway histogram equalization (MHE), nonlocal means (NLM), one-dimensional (1D) guided filtering (1D-GF) and deep learning-based stripe nonuniformity correction (DLS-NUC).

A. Quantitative Evaluation

We evaluated the performance of each NUC method by quantitatively interpreting the results using mean squared error (MSE), peak signal-to-noise ratio (PSNR), structural similarity (SSIM), and regular signal-to-noise ratio (SNR) metrics. PSNR is a globally averaged measure of the error between a denoised image and the original clean image, and a higher PSNR denotes a smaller average error. Its expression is as follows:

$$PSNR = 10 \times \log_{10}\left(\frac{{\mathrm{Max}_I}^2}{MSE}\right) \tag{8}$$

where the MSE is taken from noisy and denoised images, and $\mathrm{Max_I}$ denotes the maximum grey value of the image pixel.

SSIM is a metric used to measure the similarity between an image before and after distortion. It calculates the similarity of the image in terms of brightness $I(X,Y)$, contrast $C(X,Y)$, and structure $S(X,Y)$, and combines them into a comprehensive similarity score, known as the SSIM index. The SSIM index ranges from -1 to 1, where a value closer to 1 indicates a higher similarity between two images. The mathematical expression for the SSIM index is as follows:

$$\begin{aligned} SSIM\left(X,Y\right) &= \left[I\left(X,Y\right) \cdot C\left(X,Y\right) \cdot S\left(X,Y\right)\right]^{\sigma} \\ &= \frac{\left(2u_X u_Y + c_1\right)\left(2\sigma_{XY} + c_2\right)}{\left({u_X}^2 + {u_Y}^2 + c_1\right)\left({\sigma_X}^2 + {\sigma_Y}^2 + c_2\right)} \end{aligned} \tag{9}$$

where u_X and u_Y are the average pixel values of images X and Y, respectively, σ_X and σ_Y are their variances, σ_{XY} represents their covariance, and c_1 and c_2 are constants, σ is an exponential parameter, typically set to 1.

SNR is commonly used to assess image quality. In our simulation, noiseless IR images were used to simulate nonuniform noisy images. As such, we created a noise-free image as the ground-truth (GT). Hence, any changes in the SNR of the before and after images were used to assess the empirical denoising effects of the different methods. SNR is expressed as follows:

$$SNR = 10 \times \log_{10}\left(\frac{\mu_{sig}}{\sigma_{bg}}\right) \tag{10}$$

where μ_{sig} is the variance found in the GT image, and σ_{bg} represents the noise variance.

B. Simulation Dataset

To comprehensively evaluate the performance of different debanding algorithms, we used 80 clean IR images, 800 simulated nonuniformly noisy images with cropping and noising augmentation, and their respective GT images as qualitative and quantitative references.

As noted, the nonuniform noise of an image acquired by an IR focal plane detector usually consists of array and readout circuit interference types. Reflecting the premise of our research design, we again note that multiple IR frames acquired over a short period have essentially the same gain and bias coefficients at each pixel and readout circuit.

We modelled the probe element and redout circuit noise response curves as Gaussian functions. To simulate the probe element noise, we applied the following function:

$$DN1\,(i,j) = A\,(i,j) \times e^{-((img(i,j)-B(i,j))/\sigma(i,j))^2} + D\,(i,j) \tag{11}$$

where $img(i,j)$ is the irradiated input at the probe element (noiseless map), $DN1(i,j)$ denotes the response output of the probe element at (i,j), and $A(i,j)$, $B(i,j)$, $\sigma(i,j)$ and $D(i,j)$ are the respective probe element parameters of the response curve. We maintained the response parameters of each probe within a certain range, but they all differed. As such, we simulated the nonuniform sand noise image.

Using (11), we simulated a Gaussian response model of a four-way readout circuit as follows:

$$DN2\,(i,j) = A_n \times e^{-\left({}^{(DN1(i,j)-B_n)}/_{\sigma_n}\right)^2} + D_n\,(i,j) \tag{12}$$

where $DN1(i,j)$ denotes the irradiation input at the (i,j) probe element, $DN2(i,j)$ denotes the response output of the probe element under different readout circuits, and A_n, B_n, σ_n and $D_n(i,j)$ are the parameters of the response curves of the nth readout circuit, respectively, where $n \in [1,4]$. We ensured that the response parameters of each readout circuit remained within a certain range while not being identical. Additionally, during the readout simulation, as long as we rendered $DN1(i,j)$ as $img(i,j)$, then $DN2(i,j)$ was the only readout circuit producing stripe noise images.

C. Independent Noise Experiment

To verify the effectiveness of our nonuniform sand and stripe noise-producing method, we simulated 800 images with only sand noise, 800 images with only stripe noise and 800 IR images with both. As such, we conducted experiments on simulated sand noise images based on inhomogeneous detector element responses. Recall that the detector's response to irradiation input from the same uniform region differs at different probes, which causes the sand noise. However, this inhomogeneity remains consistent, even over short periods at the same probe element. Our method utilises this property by reordering multiple frames from the same probe, counting their uniform regions and recombining the counted row- and block-uniform regions to solve the respective linear equations described above. This provides the gain and bias coefficients for each probe, and our calibration results are shown in Fig. 5. In Fig. 5: (a) represents the original noise-free image; (b) shows the simulated probe noise image; (c) presents the correction results using our method. In (c), the first row of each column corresponds to the two-dimensional spatial object image, and the second row represents the 3D images corresponding to the objects. The simulated image affected by noise (b) becomes significantly blurred, and compared to the original noise-free image, the 3D images corresponding to (b) exhibit many protrusions, resulting in an uneven appearance. After correction, the SNR of the image in (c) improved by 5.7, while retaining fine details in the image. The 3D images in (c) have regained their smoothness and closely resemble those in (a). We also counted the changes in the average PSNR and SSIM metrics before and after denoising 800 images, in which the PSNR was 35.13 before denoising and 40.07 afterwards, and the SSIM was 0.91 before and 0.99 afterwards. Our results show that the proposed method is highly effective in correcting sand noise.

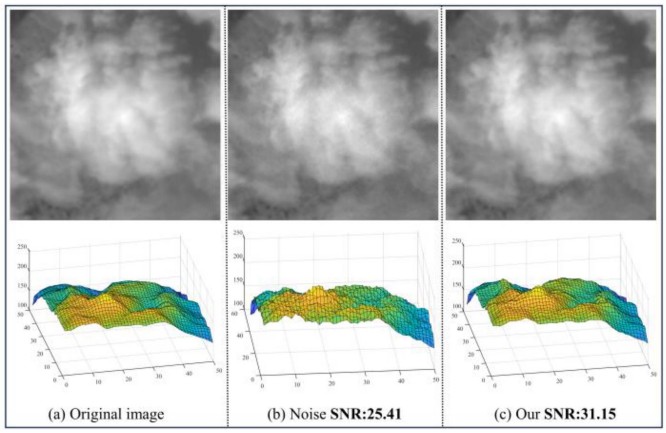

Fig. 5. Denoising results of our method on probe element nonuniform noise images.

We subsequently validated our method on striped noise images using only four readout circuits and their nonuniformity responses, meaning that they were inconsistent between columns. However, for probes with the same NUC coefficients per column, the nonuniformity was the same for different frames taken from the same probe location. The experimental results are shown in Fig. 6: (a) represents the original noise-free image; (b) displays the simulated readout circuitry noise image; (c) shows the correction results using our method. In (b), there are many striping noise compared to the original noise-free image. This noise manifests as protruding ridges in the 3D image. After correction, the SNR of the image in (c) improved by 7, and the striping noise in the image has been completely removed. A comparison between the 3D images of (c) and the original image (a) reveals that the corrected image has largely restored the same texture and shape as the original. Where the average PSNR of an image was 31 before denoising and 37.2 afterwards. The average SSIM was 0.83 before and 0.95 afterwards. These results show that our method does an outstanding job of correcting the nonuniformity of readout circuits.

TABLE I
AVERAGE/VARIANCE PSNR AND SSIM RESULTS OF DIFFERENT METHODS ON DATA1 AND DATA2 SIMULATED NOISE IR IMAGES

Methods	PSNR(dB)		SSIM	
	Data1	Data2	Data1	Data2
Striped	28.11	34.5	0.7	0.88
NLM	26.8/18.7	30.76/16.1	0.545/0.0094	0.783/0.0081
MHE	32.2/16	36.03/15.1	0.833/0.0051	0.927/0.0033
1D_GF	35/8.7	38.41/8.1	0.87/0.002	0.952/0.0018
DLS_NUC	34.1/8.5	37.94/7.8	0.85/0.0018	0.946/0.0015
Ours	**35.6/8.1**	**39.36/7.6**	**0.925/0.0009**	**0.978/0.0007**

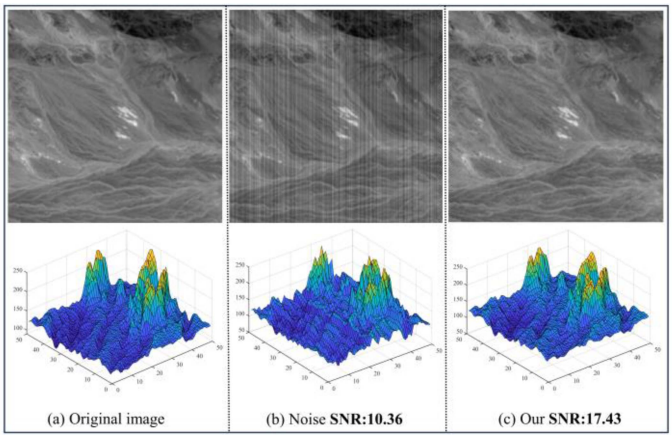

Fig. 6. Denoising results of our method on nonuniformly noisy images of readout circuits.

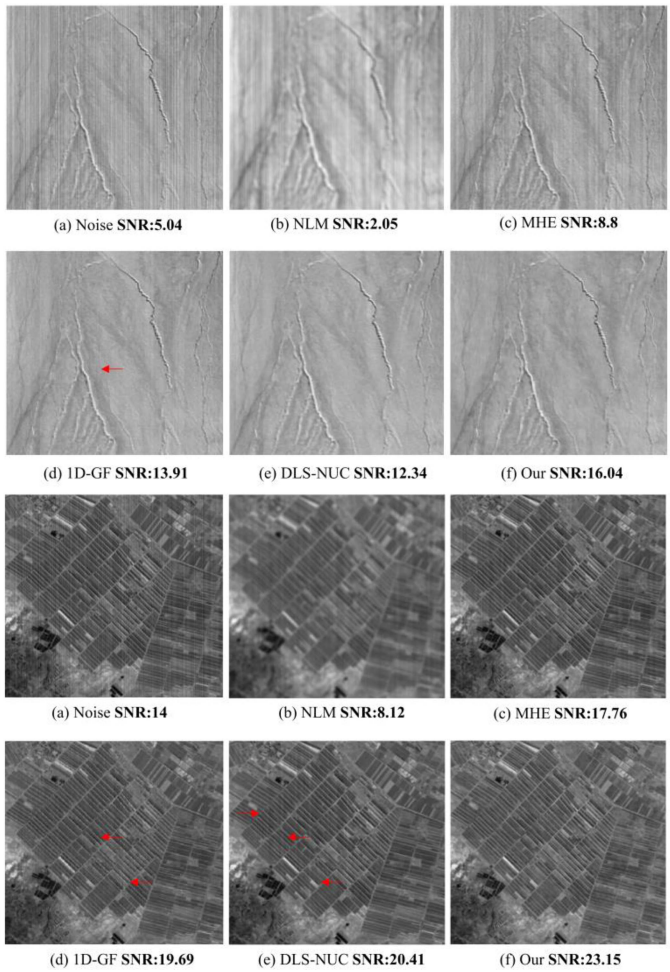

Fig. 7. NUC results using different methods: (a) noise image; (b) denoising result using NLM; (c) denoising using MHE; (d) denoising using 1D_GF; (e) denoising using DLS_NUC; (f) denoising using our algorithm.

D. Mixed Noise Comparison Experiment

Recall that the nonuniformity of both the probe element and readout circuitry results in nonuniform noise. Therefore, the correction method must be able to correct both types simultaneously. Our method applied the same steps for both noise types, and the response outputs per probe were the same over short periods. Unsurprisingly, our method was effective in both cases, as well as those of noise superpositions. Fig. 7 illustrates the correction effects of the nonuniform noise correction methods, in the figure, the residual noise locations are indicated by red arrows.

Note that the traditional the NLM denoising algorithm is too smooth, resulting in the loss of image details. In contrast, the MHE method removed some of the nonuniform noise, but not the stronger striped noise. The 1D-GF method uses a 1D line conducting filter to extract the high frequency parts of the image (i.e., stripe noise), but it could not remove low-frequency sand noise. However, the method did poorly in removing the sand noise caused by the probe element (Scene 1); this phenomenon was widespread throughout the denoising results of the entire dataset. Furthermore, due to the presence of a significant amount of horizontal texture in the object images within Scene 2, the correction applied by the 1D-GF method disrupts the texture information in the image The corrected results show that 1D-GF method retained the details while removing most of the stripe noise, which still existed in the corrected images Scene 2. The DLS-NUC method retained most of the image details while removing sand and stripe noise; however, some stripe noise remained. The method's greyscale uniformity led to differences between the original and corrected images. Scenes 1 and 2 show that our proposed method simultaneously eliminated both noise types while retaining detailed image information, which verifies its effectiveness and practicality.

Table I lists the denoising abilities of the various methods under different levels of nonuniform noise. To verify the robustness of our method under different degrees of noise, we

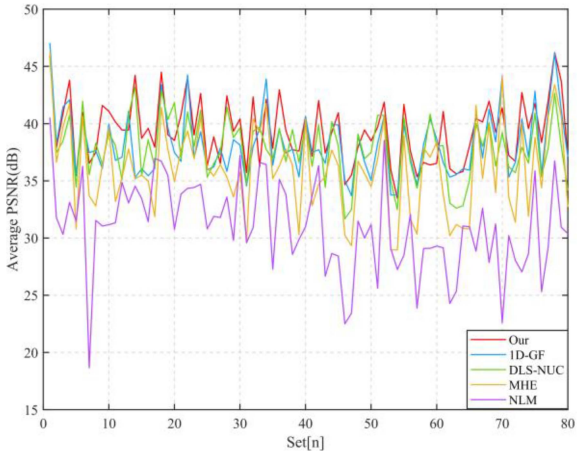

Fig. 8. Mean PSNR results statistics of different methods on Data2.

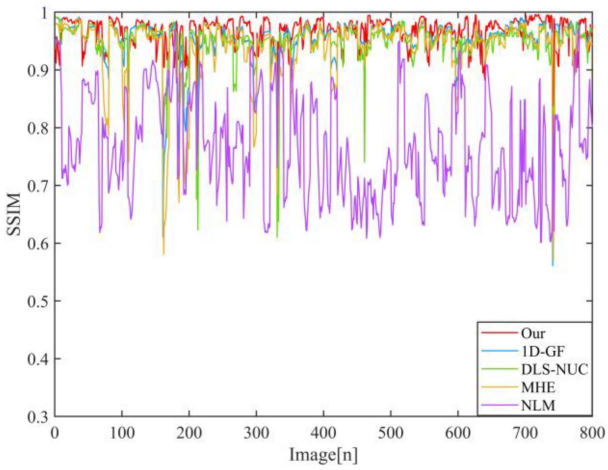

Fig. 9. Mean SSIM results statistics of different methods on Data2.

performed two noise addition experiments on 800 simulated images to obtain Data1 and Data2, from which we obtained their average/variance PSNR and SSIM values. By comparing the results of all methods, it is easy to see that our method obtained the highest scores.

To provide a more intuitive denoising demonstration, Figs. 8 and 9 display the PSNR and SSIM values of the different methods based on Data2. Owing to the large fluctuation of PSNR values from the different images, it would not be effective to display them on a single statistical graph. Noting that the 800 images comprising Data2 were cropped from 80 IR source images, we divided them into 80 groups for this presentation. It can be seen that the average PSNRs and SSIMs of MHE, 1D_GF, DLS_NUC and our method had similar overall trends; however, ours was the best.

To further evaluate the stripe noise removal ability of the different algorithms, Fig. 10 displays the column-wise averages of the post-corrected images for each method from Fig. 7 (Scene 2). Many burrs can be observed in the curves of the MHE and 1D-GF models, indicating that striping still existed in their results. The outputs of the DLS-NUC and NLM methods clearly deviated

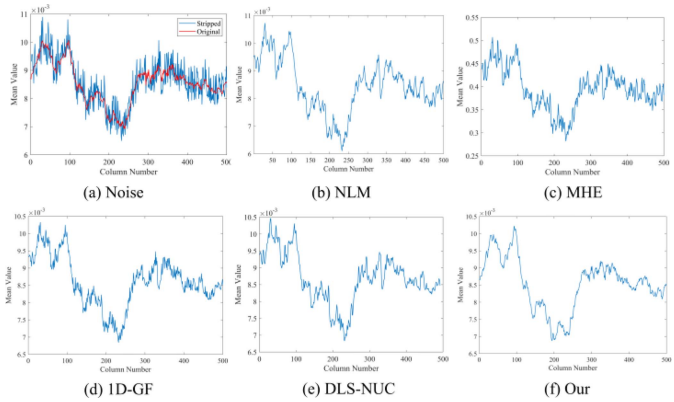

Fig. 10. Column mean curves of de-striping results of different methods on Scene 2 images.

from the actual results. On the other hand, our method provided the best agreement with the GT results, demonstrating clear superiority.

This section demonstrates the correction effects of different methods on image nonuniformity through a large number of experiments. Among these methods, NLM and MHE show very limited correction performance for nonuniform noise and may even degrade the fine details in the image during the correction process. Consequently, these two methods yield low values for both PSNR and SSIM metrics. The 1D-GF algorithm effectively eliminates striping noise in the image but may potentially disrupt details in object images with horizontal and vertical textures, and it cannot remove probe element nonuniformity noise. The DLS_NUC algorithm, which learns to simultaneously correct both probe element nonuniformity and readout circuitry nonuniformity, exhibits over-optimization of the image, leading to the distortion of grayscale levels in the correction results. The correction method proposed in this paper demonstrates superior correction performance and stable performance throughout the entire experiment. It not only corrects nonuniformities but also restores the column-wise mean curve of the image.

E. Experiments on Real Stripe Noise Images

To verify the effectiveness of our method, we performed nonuniform correction experiments on blackbody radiation and outlook imaging data collected by our detector. The results are shown in Figs. 11 and 12, where it can be seen that the MHE and NLM methods did not effectively eliminate the nonuniform noise. Moreover, they destroyed the detailed information. The 1D-GF method effectively removed the bands, but artifacts appeared in the corrected result (Fig. 11), and sand noise was still present in the corrected result of Fig. 12. The results of the depth-based DLS-NUC method (Fig. 11) were severely corrupted, and the image in Fig. 12 was obviously enhanced with its correction. However, this destroyed the original greyscale information. In contrast, our correction results shown in Figs. 11 and 12 reveal clearly removed FPN without the loss of original information.

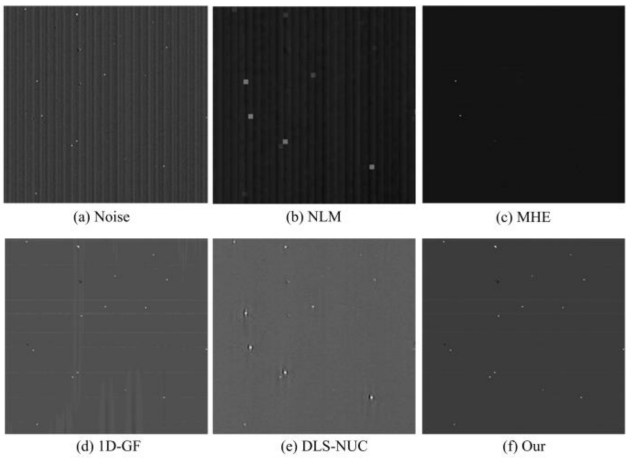

Fig. 11. Correction results for blackbody radiation images.

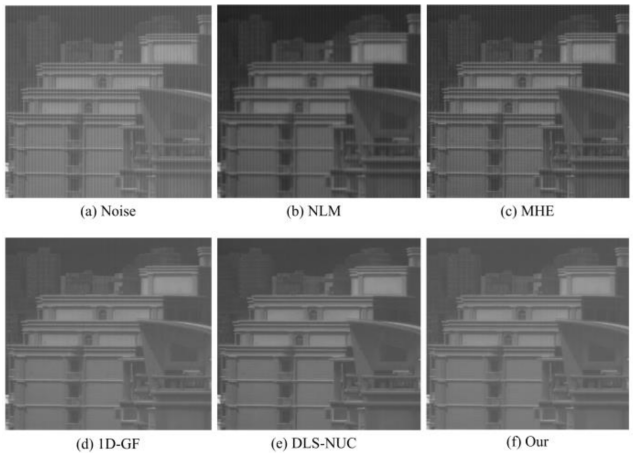

Fig. 12. Correction results for exterior imaging data.

V. Conclusion

In this study, an effective nonuniform noise correction method was proposed. Compared with existing methods, ours removes both sand and stripe noise types caused by multiple detector probes and readout circuits without blurring or destroying image details. Additionally, our method effectively overcomes the effects of detector response nonlinearity while making full use of the cause and nature of the nonuniform noise based on small time frames. First, multiple frames are acquired by the detector over a short period and are rearranged according to their corresponding pixel positions. The pixel values of different frames from the same detectors are calculated, and a multi-segment linear model is constructed to extract their nonuniform correction coefficients. These are then applied to the noisy images for correction. We compared our results with four existing scene-based NUC methods, and the results clearly show that our method is superior. In summary, the proposed model removes nonuniform noise while preserving the detailed information of IR images without false artifact generation. Incredibly, the method is stable when correcting IR images from different scenes while preserving the column mean curve of the image during denoising.

References

[1] M. Schulz and L. Caldwell, "Nonuniformity correction and correctability of infrared focal plane arrays," *Infrared Phys. Technol.*, vol. 36, pp. 763–777, 1995, doi: 10.1016/1350-4495(94)00002-3.
[2] C. L. Liu et al., "Non-uniformity correction algorithm for IRFPA based on motion controllable micro-scanning and perimeter diaphragm strips," *Optik*, vol. 122.19, pp. 1764–1769, 2011, doi: 10.1016/j.ijleo.2010.10.040.
[3] Y. Tendero, J. Gilles, S. Landeau, and J. M. Morel, "Efficient single image nonuniformity correction algorithm," *Proc. SPIE*, vol. 7834, pp. 96–107, 2010, doi: 10.1117/12.864804.
[4] Y. Cao, M. Y. Yang, and C. L. Tisse, "Effective strip noise removal for low-textured infrared images based on 1-D guided filtering," *IEEE Trans. Circuits Syst. Video Technol.*, vol. 26, no. 12, pp. 2176–2188, Dec. 2016, doi: 10.1109/TCSVT.2015.2493443.
[5] Y. Tendero, S. Landeau, and J. Gilles, "Nonuniformity correction of infrared images by midway equalization," *Image Process. Line.*, vol. 2, pp. 134–146, 2012, doi: 10.5201/ipol.2012.glmt-mire.
[6] K. Chen, "Key Technologies research of information acquisition and processing in long-wave infrared hyperspectral imaging," *IEEE Geosci. Remote Sens. Mag.*, vol. 7, no. 2, pp. 72–100, 2016.
[7] K. Dabov, A. Foi, V. Katkovnik, and K. Egiazarian, "Image denoising by sparse 3-D transform-domain collaborative filtering," *IEEE Trans. Image Process.*, vol. 16, no. 8, pp. 2080–2095, Aug. 2007, doi: 10.1109/tip.2007.901238.
[8] Z. He, Y. Cao, Y. Dong, J. Yang, Y. Cao, and C. L. Tisse, "Single-image-based nonuniformity correction of uncooled long-wave infrared detectors: A deep-learning approach," *Appl. Opt.*, vol. 57, pp. D155–D164, 2018, doi: 10.1364/AO.57.00D155.
[9] E. Vera, P. Meza, and S. Torres, "Total variation adaptive scene-based nonuniformity correction," in *Proc. Imag. Syst.*, 2010, Paper JTuA24, doi: 10.1364/IS.2010.JTuA24.
[10] R. C. Hardie et al., "Scene-based nonuniformity correction with video sequences and registration," *Appl. Opt.*, vol. 39, no. 8, pp. 1241–1250, 2000, doi: 10.1364/AO.39.001241.
[11] Z. Zhuang and H. Wang, "A novel nonuniformity correction algorithm based on speeded up robust features extraction," *Infrared Phys. Technol.*, vol. 73, pp. 281–285, 2015, doi: 10.1016/j.infrared.2015.10.006.
[12] H. Ji, "Research on the technology of high sensitivity and high spectral image information processing," *BMC Neurosci.*, vol. 17, pp. 54, 2016.
[13] Y. Cao and Y. Li, "Strip nonuniformity correction in uncooled long-wave infrared focal plane array based on noise source characterization," *Opt. Commun.*, vol. 339, pp. 236–242, 2015, doi: 10.1016/j.optcom.2014.10.041.
[14] Y. Bae, J. Lee, J. H. Lee, and J. B. Ra, "Scene-based nonuniformity correction in infrared videos," Proc. *SPIE*, vol. 8399, pp. 137–145, 2012, doi: 10.1117/12.919049.
[15] X. Sui, Q. Chen, and G. Gu, "Adaptive greyscale adjustment-based stripe noise removal method of single image," *Infrared Phys. Technol.*, vol. 60, pp. 121–128, 2013, doi: 10.1016/j.infrared.2013.04.006.
[16] E. Wang, P. Jiang, X. Li, and H. Cao, "Infrared stripe correction algorithm based on wavelet decomposition and total variation-guided filtering," *J. Eur. Opt. Soc.-Rapid Publ.*, vol. 16, pp. 1–12, 2020, doi: 10.1186/s41476-019-0123-2.
[17] S. N. Torres and M. M. Hayat, "Kalman filtering for adaptive nonuniformity correction in infrared focal-plane arrays," *J. Opt. Soc. Amer. A Opt. Image Sci. Vis.*, vol. 20, pp. 470–480, 2003, doi: 10.1364/josaa.20.000470.
[18] J. Guan, R. Lai, and A. Xiong, "Wavelet Deep Neural network for stripe noise removal," *IEEE Access*, vol. 7, pp. 44544–44554, Mar. 2019, doi: 10.1109/ACCESS.2019.2908720.
[19] D. Ding et al., "Single infrared image stripe removal via residual attention network," *Sensors*, vol. 22, 2022, Art. no. 8734, doi: 10.3390/s22228734.
[20] Q. Song, Y. Wang, X. Yan, and H. Gu, "Remote sensing images stripe noise removal by double sparse regulation and region separation," *Remote Sens.*, vol. 10, 2018, Art. no. 998, doi: 10.3390/rs10070998.
[21] Q. Zeng, H. Qin, X. Yan, S. Yang, and T. Yang, "Single infrared image-based stripe nonuniformity correction via a two-stage filtering method," *Sensors*, vol. 18, 2018, Art. no. 4299, doi: 10.3390/s18124299.
[22] Y. Shao et al., "Infrared image stripe noise removing using least squares and gradient domain guided filtering," *Infrared Phys. Technol.*, vol. 119, 2021, Art. no. 103968, doi: 10.1016/j.infrared.2021.103968.
[23] B. L. Hu, S. J. Hao, D. X. Sun, and Y. Liu, "A novel scene-based nonuniformity correction method for SWIR push-broom hyperspectral sensors," *ISPRS J. Photogramm.*, vol. 131, pp. 160–169, 2017, doi: 10.1016/j.isprsjprs.2017.08.004.